PERGAMON

International Journal of Heat and Mass Transfer 44 (2001) 2093–2106

International Journal of HEAT and MASS TRANSFER

www.elsevier.com/locate/ijhmt

Freezing of a porous medium in contact with a concentrated aqueous freezant: numerical modelling of coupled heat and mass transport

T. Lucas [a,*], J.M. Chourot [a], Ph. Bohuon [b], D. Flick [c]

[a] *Cemagref, Refrigeration Process Engineering Research Unit, P.O. Box 44, F-92163 Antony Cedex, France*
[b] *CIRAD-ENSIA, Process Engineering and Equipment Research Unit, 73, rue J.F. Breton, BP 5035, F-34032 Montpellier, France*
[c] *INAPG, Fluid Dynamics and Transport Phenomena Research Unit, 16 rue Claude Bernard, F-75231 Paris Cedex 5, France*

Received 10 June 1999; received in revised form 26 June 2000

Abstract

The authors have developed a model of coupled heat and mass transport within a porous medium (sheet) saturated with an aqueous solution of initial non-zero solute concentration. The novel contribution of the present work is the resolution of the equations for simultaneous heat and mass flows at one of the interfaces for a wide range of temperatures and concentrations. Good agreement was noted between the simulated and the experimental data. The results presented also underline the fact that this knowledge model helps to clarify our understanding of the interaction mechanisms between heat and mass transport during the immersion freezing process.

Keywords: Glass bead; NaCl; Thawing; Immersion freezing

1. Introduction

The study of heat and mass transfer with phase change (freezing) within a porous medium saturated with an aqueous solution is of interest to various fields of application. For instance:

- in soil science, subsea permafrost thaws relatively slowly but to a gradually increasing depth; thawing is associated with the existence of differences both in temperature and in sodium chloride concentration between the seawater and the permafrost [1];
- in cryobiology, one of the factors determining the survival rate of frozen embryos is the control of heat and mass transfer between the tissues and the freezing medium containing cryoprotective agents [2];
- in food technology, immersion freezing of foodstuffs in direct contact with concentrated aqueous solutions (e.g. brine) is a rapid individual quick freezing (IQF) process. The process has not been developed to any great extent because of difficulty in controlling solute impregnation; however a revival of interest is apparent with the appearance of new food products, i.e. preformulated frozen products [3].

Although heat transfer is more rapid than mass transfer and thermal equilibrium is established well before mass equilibrium, the two types of transport are nevertheless closely linked when they develop within a porous medium. Coupling occurs through a variety of different mechanisms:

(i) In the media studied (saline soil, cell tissues), initial concentration, $\omega_{l_0}^{\ell}$, is non-zero. This means that while the medium is in the course of freezing, the solute concentration of the remaining liquid phase (ω_l^{ℓ}) increases (cryo-concentration) and its freezing temperature ($T_{\mathrm{sat}}\{\omega_l^{\ell}\}$) decreases. The medium contains a liquid region (as yet unfrozen, with $\omega_l^{\ell} = \omega_{l_0}^{\ell}$), a 'mushy' region ($\omega_l^{\ell}$ variable with the position and time) and a completely frozen region.

* Corresponding author. Tel.: +33-2-23-48-21-77; fax: +33-2-23-48-21-15.
E-mail address: tiphaine.lucas@cemagref.fr (T. Lucas).

0017-9310/01/$ - see front matter
PII: S0017-9310(00)00238-6

Nomenclature

A variable used in the numerical resolution of Eqs. (35)–(37)
B variable used in the numerical resolution of Eqs. (35)–(37) (°C^{-1})
C specific heat (J kg^{-1} K^{-1})
$\omega^{\ell}_{1_0}$ effective diffusion coefficient of NaCl within the porous medium (m^2 s^{-1})
$D^{\ell}_{1/2}$ mutual diffusion coefficient of water and NaCl in the liquid phase (m^2 s^{-1})
$D^{\ell}_{1/2_\bullet}$ mutual diffusion coefficient of water and NaCl at infinite dilution (m^2 s^{-1})
e freezing front position from interface porous medium/external solution (m)
H partial mass enthalpy (J kg^{-1})
h heat transfer coefficient (W m^{-2} K^{-1})
ΔH latent heat of fusion of ice (J kg^{-1})
K mass transfer coefficient (m s^{-1})
k thermal conductivity (W m^{-1} K^{-1})
L height of the porous medium (m)
$\mathring{m}_2$ water crystallisation mass rate (kg m^{-3} s^{-1})
T temperature (°C)
T_{sat} liquidus curve function (°C)
t time (s)
Δt time step in finite difference calculations (s)
X thawing front position from interface porous medium/external solution (m)
x Cartesian coordonate in an upwards direction (perpendicular to flow) (m). $x=0$ at the interface porous medium/external solution
Δx space step in finite difference calculations (m)
y Cartesian coordonate in a lengthwise direction (parallel to flow) (m). $y=0$ at the inlet
z Cartesian coordonate in the porous medium in a widthwise direction (tangential to flow) (m) $z=0$ at the porous medium/refrigerating solution interface

Greek symbols

β constant used in Eq. (20) (°C)
ε porosity of the solid matrix
$\vec{\eta}_i$ flow of component i through the porous medium (kg m^{-2} s^{-1})
μ dynamic viscosity (Pa s)
ρ density (kg m^{-3})
τ tortuosity of the solid matrix
ω mass fraction
ω_{sat} inverse function of T_{sat}

Subscripts

E Eutectic
ℓ liquid phase
j node in the numerical scheme ($1 < j < j\max$)
m porous medium
n time in the numerical scheme
s solid phase
0 initial moment in the porous medium
1 solute, in the context of application solute is NaCl
2 liquid water
3 ice
4 glass beads
∞ external solution

Superscripts

0 identifies the reference for enthalpy calculation
m identifies a quantity associated with the porous medium
ℓ identifies a quantity associated with the liquid phase
+ identifies a quantity associated with the liquid + ice phases

(ii) Cryoconcentration induces a concentration gradient between the mushy region and the completely liquid region; this is reflected in solute redistribution and enrichment of the liquid region at the expense of the mushy region.
(iii) The convection or bulk flow engendered by ice expansion induces mass transport. This phenomenon represents about 9% of the rate of advance of the freezing front [4].
(iv) The difference in density between the solution in the mush (high concentration, low temperature) and that in the completely liquid region (low concentration, high temperature) induces convective transport, of significant proportions if the freezing front travels in a downwards (i.e. in the direction of the earth's gravity).
(v) A thermal gradient within the porous medium can engender mass transport (Soret effect), or vice versa (Dufour effect).
(vi) The thermodynamic properties (e.g. enthalpy of the medium) and transport properties are a function of both the temperature and the composition of the medium. They are also very sensitive to the ice fraction. In particular, the area available for diffusion is reduced by the presence of ice, with a linear decrease in the effective coefficient of diffusion as the ice fraction increases.
(vii) At the porous medium/external solution interface, interaction between heat and mass transfer affects the nature of heat and mass transport within the porous medium.

Existing coupled heat and mass transfer models incorporate one or more of these phenomena, but rarely all. In this introduction phenomena (iv) and (v) will not be further studied and discussed.

Mass transport has been coupled with heat transport during the freezing of a concentrated aqueous solution ($\omega^{\ell}_{1_0} \neq 0$) as a free medium, e.g. [5–7]. In such models, the system studied never includes mass transfer at the interface. Only cryo-concentration (i) and redistribution (ii) are considered [5]; mass transport following ice expansion may also be taken into account [6,7]. The thermophysical and transport properties are also temperature- and concentration-dependent phenomenon (vi) [5–7]. It is difficult to validate the models experimentally, as sampling of the solution is virtually impossible during freezing beyond a certain ice fraction and the concentration differences in any profile are low. Only Jochem and Korber [5] present an experimental validation of solute redistribution after the freezing of a water–NaCl solution. The phenomena are well reproduced, although solute redistribution appears to be underestimated. Experimental measurement of mass transport is at present not precise enough to determine the respective contributions of the various possible mechanisms, e.g. the increase in crystal size or bulk flow [5–7].

Other models, applied to the thawing of permafrosts, couple mass and heat transport within a semi-infinite porous medium, saturated with frozen pure water ($\omega^{\ell}_{1_0} = 0, T_0$) and in contact with a concentrated aqueous solution ($\omega^{\ell}_{1_\infty} \geqslant \omega^{\ell}_{1_0},\ T_\infty \geqslant T_0$). The system studied and the phenomena examined are presented diagrammatically in Fig. 1(b). One feature considered is discontinuity of the ice mass fraction, ω^{+}_{3} (or thawing front) between the completely thawed region ($\omega^{+}_{3} = 0$) and the completely frozen region ($\omega^{+}_{3} = 1$). Formulated in this way, the problem is simply a generalisation of the Neuman problem [8]. It has been developed by Harrison and Osterkamp [9] and others. Heat and mass transports are coupled at the freezing front by the liquidus equation. To simplify resolution, the liquidus curve is assumed to be linear and the temperature and concentration ranges considered within the system are therefore very small ($\Delta T \leqslant 4°C,\ \Delta\omega^{\ell}_{1} \leqslant 0.05$). Experimental validation of the model against permafrost is hampered by inadequate knowledge of the transport properties in such complex media.

Vasil'ev et al. [10] have developed the generalised Neuman problem, replacing the completely frozen region ($\omega^{\ell}_{1_0} = 0$) by a partially frozen (mushy) region (Fig. 1(c)). Solute diffusion also occurs in the liquid

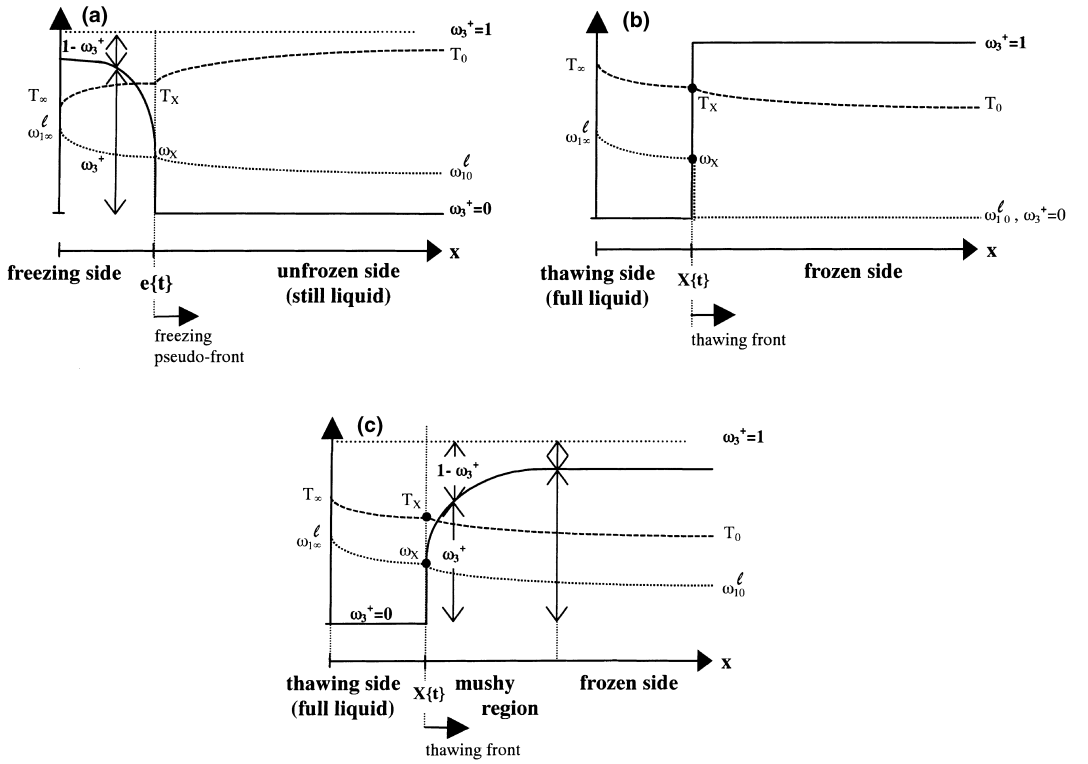

Fig. 1. Approaches to coupled transfer modelling in the literature: (a) Jochem and Korber [5]; (b) Harrison and Osterkamp [9]; (c) Vasil'ev [10].

phase of the mush, and the liquidus equation linking T and ω_1^ℓ is valid for all the mush. For the purposes of analytical resolution, the authors linearise the mass equation, complementing the hypotheses already advanced by Harrison and Osterkamp [9]. In the presented simulations, both cases $T_\infty > T_0$ and $T_\infty < T_0$ were considered, with $\omega_{1_\infty}^\ell \geqslant \omega_{1_0}^\ell$.

In this paper these authors consider a porous medium saturated with a dilute water–solute solution. Initially the system is at uniform temperature (T_0) and solute concentration ($\omega_{1_0}^\ell$). At time $t = 0$, the porous medium is put in contact with a concentrated binary water–solute solution ($\omega_E > \omega_{1_\infty}^\ell > \omega_{1_0}^\ell$, $T_E < T_\infty \leqslant T_0$). This initiates the chilling and freezing process and solute diffusion from the surface inwards. The aim of the present work was to develop a model of coupled heat and mass transport that could be used to predict both the freezing and the thawing phenomena of a porous medium of finite dimensions (slab). In comparison to the existing models, the main advances are consideration of convective heat and mass flows at the porous medium/concentrated solution interface and resolution of the model for a wide range of temperatures and concentrations. The first part presents the equations of the model and the simplifying assumptions. The second part compares simulations using the model with both the existing analytical solutions and our own experimental data.

2. Heat and mass transfer model

Structure of the studied system and main assumptions were the following:

(A1) A porous medium comprising a solid matrix and a saturating dilute water–solute solution was under consideration. The solid matrix of porosity ε was assumed to be inert (e.g. no chemical reactions with the saturating phase(s)) and not to undergo any deformation. The whole system was considered as a continuum.

(A2) All phases were at the same temperature and local phase equilibrium in the mushy region was valid (referring to equilibrium phase diagram). Supercooling phenomena were not taken into account.

(A3) The solute concentration in both the external solution and the solution saturating the porous medium, is considered lower than the eutectic concentration given by the state diagram of the water–solute system. Their temperature is also considered higher than the corresponding eutectic temperature. This implies that (i) only water may crystallise (no possible crystallisation of solute); (ii) that whatever the temperature in the porous medium, it always persists some liquid phase.

(A4) The densities of the water–solute solution (ρ_ℓ), the ice (ρ_3) and the beads (ρ_4) were constant. The volume change associated with ice–water phase transition (about 9%) was neglected ($\rho_\ell = \rho_3 = 1000$ kg m^{-3}).

(A5) Mass transport took place only in the liquid phase (no transport of either the solid matrix or the ice crystals).

(A6) The problem is solved numerically for the case of a slab (one-dimensional treatment). The surface at $x = 0$ is put in contact with the external solution; at the other one ($x = L$), all flows equal to zero.

In such conditions, the macroscopic equations governing heat and mass transport phenomena were:

2.1. Mass conservation

The mass conservation equations presented in Table 1 are written for each component in each phase [11]. ρ_i^m is the density of component i in the porous medium (kg i per m^3 of porous medium); η_i^m, the flow of component i (kg i per m^2 of porous medium and per unit of time); $\mathring{m}_2$, the water crystallisation mass rate per m^3 of porous medium and per unit of time.

Adding Eqs. (1)–(4) results in Eq. (5):

$$\frac{\partial}{\partial t}(\rho_m) + \nabla \cdot (\vec{\eta}_1^m + \vec{\eta}_2^m) = 0, \tag{5}$$

where ρ_m is the effective density of the porous medium ($\rho_m = \rho_1^m + \rho_2^m + \rho_3^m + \rho_4^m$).

By definition

$$\vec{\eta}_\ell^m = \vec{\eta}_1^m + \vec{\eta}_2^m. \tag{6}$$

Eq. (5) can now be written as:

$$\frac{\partial}{\partial t}(\rho_m) + \nabla \cdot (\vec{\eta}_\ell^m) = 0. \tag{7}$$

On the basis of assumptions (A4) and (A6), ρ_m is constant and $\vec{\eta}_\ell^m = 0$ at $x = L$, so according to Eq. (7) the

Table 1
Summary of mass conservation equations

Phase	Component (i)	Mass conservation equation	
Liquid (ℓ)	Solute (1)	$\frac{\partial \rho_1^m}{\partial t} + \nabla \cdot \left(\vec{\eta}_1^m\right) = 0$	(1)
	Water (2)	$\frac{\partial \rho_2^m}{\partial t} + \nabla \cdot \left(\vec{\eta}_2^m\right) = -\mathring{m}_2$	(2)
Solid (s)	Ice (3)	$\frac{\partial \rho_3^m}{\partial t} = \mathring{m}_2$	(3)
	Glass beads (4)	$\frac{\partial \rho_4^m}{\partial t} = 0$	(4)

mean velocity of the liquid phase is zero at all points in the medium.

2.2. Mass transport equation

Mass (liquid water and solute) transport in the liquid phase is thus purely diffusional and does not include convective transport. The mass transport equation is developed for the solute according to Fick's law of diffusion [11]

$$\vec{\eta}_1^{\mathrm{m}} = -\rho_\ell^{\mathrm{m}} D_{1/2}^{\mathrm{m}} \nabla(\omega_1^\ell), \tag{8}$$

where $D_{1/2}^{\mathrm{m}}$ is the effective diffusion coefficient of the solute within the porous medium. Eq. (1) can now be rewritten taking into account Eq. (8)

$$\frac{\partial \rho_1^{\mathrm{m}}}{\partial t} - \nabla \cdot \left(\rho_\ell^{\mathrm{m}} D_{1/2}^{\mathrm{m}} \nabla(\omega_1^\ell) \right) = 0. \tag{9}$$

2.3. Energy conservation equation

The equation for changes in temperature, T, is derived from the energy balance per unit of volume. Only heat conduction is under consideration and the well-known Fourier's law is applied (i.e. we assume no work done by gravitational, viscous or pressure forces, nor heat of dilution)

$$\frac{\partial}{\partial t}\left(\rho_1^{\mathrm{m}} H_1 + \rho_2^{\mathrm{m}} H_2 + \rho_3^{\mathrm{m}} H_3 + \rho_4^{\mathrm{m}} H_4\right) = \nabla \cdot (k_{\mathrm{m}} \nabla T) - \nabla \cdot \left(H_1 \eta_1^{\mathrm{m}} + H_2 \eta_2^{\mathrm{m}}\right). \tag{10}$$

Here k_{m} is the effective thermal conductivity of the porous medium, and $H_{i\in[1,2,3,4]}$ is the partial mass enthalpy of component i. The latter is expressed as $H_i = H_i^0 + C_i(T - T^0)$, where H_i^0 is the partial mass enthalpy at the reference temperature T^0 taken at 0°C. The specific heat values are considered to be independent of temperature and solute concentration (A7).

By replacing the full expressions of the partial mass enthalpies into Eq. (10) and using the mass conservation Eqs. (1)–(4), it gives after simplification

$$\frac{\partial}{\partial t}\left((\rho C)^{\mathrm{m}} T\right) - \left(H_2^0 - H_3^0\right)\mathring{m}_2 = \nabla.(k_{\mathrm{m}} \nabla T) - \nabla \cdot \left(C_1 T \eta_1^{\mathrm{m}} + C_2 T \eta_2^{\mathrm{m}}\right). \tag{11}$$

Here

$$(\rho C)^{\mathrm{m}} = \rho_1^{\mathrm{m}} C_1 + \rho_2^{\mathrm{m}} C_2 + \rho_3^{\mathrm{m}} C_3 T + \rho_4^{\mathrm{m}} C_4. \tag{12}$$

The enthalpy of fusion of ice is defined as $\Delta H = H_2^0 - H_3^0$ at the reference temperature $T^0 = 0$°C. By replacing Eqs. (3) and (12) into Eq. (11), it gives

$$\frac{\partial}{\partial t}\left(\rho_1^{\mathrm{m}} C_1 T + \rho_2^{\mathrm{m}} C_2 T + \rho_3^{\mathrm{m}} (C_3 T - \Delta H) + \rho_4^{\mathrm{m}} C_4 T\right) = \nabla \cdot (k_{\mathrm{m}} \nabla T) - \nabla \cdot \left(C_1 T \eta_1^{\mathrm{m}} + C_2 T \eta_2^{\mathrm{m}}\right). \tag{13}$$

Here

$$\rho_1^{\mathrm{m}} C_1 + \rho_2^{\mathrm{m}} C_2 = \rho_l^{\mathrm{m}} (\omega_1^\ell C_1 + \omega_2^\ell C_2) = \rho_\ell^{\mathrm{m}} C_\ell,$$

which leads to reformulate Eq. (13) as follows

$$\frac{\partial}{\partial t}\left(\rho_\ell^{\mathrm{m}} C_\ell T + \rho_3^{\mathrm{m}} (C_3 T - \Delta H) + \rho_4^{\mathrm{m}} C_4 T\right) = \nabla \cdot (k_{\mathrm{m}} \nabla T) - \nabla \cdot \left(T\left(C_1 \eta_1^{\mathrm{m}} + C_2 \eta_2^{\mathrm{m}}\right)\right), \tag{14}$$

where

$$C_\ell = \omega_1^\ell C_1 + \omega_2^\ell C_2 = C_2 + \omega_1^\ell (C_1 - C_2). \tag{15}$$

We assume that C_ℓ is independent of ω_1^ℓ (A8), which is the equivalent of writing

$$C_2 \gg \omega_1^\ell (C_1 - C_2) \tag{16}$$

and, by substituting Eq. (16) into Eq. (15), we obtain

$$C_\ell = C_2. \tag{17}$$

This result will be taken into account when carrying out the numerical application.

The convective term can be expressed as

$$T\left(C_1 \eta_1^{\mathrm{m}} + C_2 \eta_2^{\mathrm{m}}\right) = \left(C_2\left(\eta_1^{\mathrm{m}} + \eta_2^{\mathrm{m}}\right) + (C_1 - C_2)\eta_1^{\mathrm{m}}\right) T. \tag{18}$$

As previously demonstrated, $\eta_1^{\mathrm{m}} + \eta_2^{\mathrm{m}} = 0$. We additionally assume that the term $(C_1 - C_2)\eta_1^{\mathrm{m}}$ from Eq. (18) can be neglected when compared to $\nabla \cdot (k_{\mathrm{m}} \nabla T)$ from Eq. (14) (A9). Let us point out that this new assumption remains consistent with previous Assumption (A8). Thus the convective term equals zero.

Eq. (13) can now be rewritten as

$$\frac{\partial}{\partial t}\left(\rho_\ell^{\mathrm{m}} C_\ell T + \rho_3^{\mathrm{m}} (C_3 T - \Delta H) + \rho_4^{\mathrm{m}} C_4 T\right) = \nabla \cdot (k_{\mathrm{m}} \nabla T). \tag{19}$$

2.4. Thermodynamic relation

The thermodynamic relation between temperature and solute concentration in the presence of ice is described by a second-order polynomial equation (A10)

$$T_{\mathrm{sat}}\left\{\omega_1^\ell\right\} = \beta_1 + \beta_2 \cdot \omega_1^\ell + \beta_3 \cdot (\omega_1^\ell)^2. \tag{20}$$

2.5. Initial and boundary conditions

At $t = 0$, solute concentration and temperature are constant inside the medium

$$\omega_1^\ell\{x, t = 0\} = \omega_{1_0}^\ell > 0, \tag{21}$$

$$T\{x, t = 0\} = T_0 > 0\text{°C (no ice)}. \tag{22}$$

At $x = L$, one can write an adiabatic and impervious condition

$$\nabla(\omega_1^\ell) = 0, \tag{23}$$

$$\nabla T = 0. \tag{24}$$

At the medium/external solution interface ($x = 0$), heat and mass fluxes are given by the heat and mass transfer coefficients (noted h and K, respectively)

$$\rho_{\ell_\infty} K\left(\omega_{1_\infty}^\ell - \omega_1^\ell\{x = 0, t\}\right) = -\rho_\ell^{\mathrm{m}} D_{1/2}^{\mathrm{m}} \nabla(\omega_1^\ell), \tag{25}$$

$$h(T_\infty - T\{x = 0, t\}) = -k_{\mathrm{m}} \nabla T. \tag{26}$$

2.6. Numerical solution

The equations set (9), (19), (20) described earlier is rewritten before being discretised into one-dimensional elements and then integrated by numerical calculation. Using Table 2, the new formulation results in a set of three main Eqs. (32)–(34) that can be used to evaluate the changes in the three independent variables selected: temperature (T), the solute mass fraction in the liquid phase (ω_1^ℓ) and the ice mass fraction in the ice–liquid mixture (ω_3^+).

$$\frac{\partial}{\partial t}\left(\rho_\ell \varepsilon (1 - \omega_3^+)\omega_1^\ell\right) = \frac{\partial}{\partial x}\left(\rho_\ell \varepsilon (1 - \omega_3^+) D_{1/2}^{\mathrm{m}} \frac{\partial \omega_1^\ell}{\partial x}\right), \tag{32}$$

$$\frac{\partial}{\partial t}\left[\rho_4(1 - \varepsilon)C_4 T + \rho_\ell \varepsilon\left((1 - \omega_3^+)C_\ell T + \omega_3^+(C_3 T - \Delta h)\right)\right] = \frac{\partial}{\partial x}\left(k_{\mathrm{m}} \frac{\partial T}{\partial x}\right), \tag{33}$$

$$T = \beta_1 + \beta_2 \cdot \omega_1^\ell + \beta_3 \cdot (\omega_1^\ell)^2 \quad \text{if } \omega_3^+ > 0. \tag{34}$$

The equations set is solved by a finite differences method. The calculation domain is covered by a network of nodes, N_j, around which control volumes are constructed. Because of the high nonlinearity of the system, a fully explicit scheme was implemented. Using such scheme for the present case of application implies $\Delta t/(\Delta x)^2 < 0.7\ 10^6$, and is thus time-consuming. In the case of the simulations presented in this paper, with $\Delta t = 0.05$ s and $\Delta x = 0.5$ mm, the calculation lasts one-tenth of the simulated time.

Table 2
Density of components i and of the liquid phase in the porous medium

Solute (1)	$\rho_1^{\mathrm{m}} = \rho_\ell \varepsilon (1 - \omega_3^+)\omega_1^\ell$	(27)
Water (2)	$\rho_2^{\mathrm{m}} = \rho_\ell \varepsilon (1 - \omega_3^+)\omega_2^\ell$	(28)
Liquid (l)	$\rho_l^{\mathrm{m}} = \rho_\ell \varepsilon (1 - \omega_3^+)$	(29)
Ice (3)	$\rho_3^{\mathrm{m}} = \rho_\ell \varepsilon \omega_3^+$	(30)
Glass beads (4)	$\rho_4^{\mathrm{m}} = \rho_4 (1 - \varepsilon)$	(31)

The value of any physical quantity Φ at node N_j and time $t + \Delta t$ is denoted Φ_j^{n+1}. Eqs. (32)–(34) are developed as follows:

$$\left(1 - \lfloor \omega_3^+ \rfloor_j^{n+1}\right) \lfloor \omega_1^\ell \rfloor_j^{n+1} = A_j^n, \tag{35}$$

$$B_{1j}^n T_j^{n+1} + B_{2j}^n T_j^{n+1} \lfloor \omega_3^+ \rfloor_j^{n+1} + B_{3j}^n \lfloor \omega_3^+ \rfloor_j^{n+1} = B_{4j}^n, \tag{36}$$

$$T_j^{n+1} = \beta_1 + \beta_2 \cdot \lfloor \omega_1^\ell \rfloor_j^{n+1} + \beta_3 \cdot \left(\lfloor \omega_1^\ell \rfloor_j^{n+1}\right)^2 \quad \text{if } \lfloor \omega_3^+ \rfloor_j^{n+1} > 0, \tag{37}$$

where A_j^n and $B_{i\in[1,2,3,4],j}^n$ are known (refer to Appendix A for details on the expression of these coefficients).

Before the first ice crystal appears or after the last ice crystal disappears, $\lfloor \omega_3^+ \rfloor_j^{n+1}$ is forced to zero and only the first two equations in the system (35) and (36) are taken into account to calculate changes in temperature and in the solute mass fraction. The equations are then coupled only by the transport properties. During cooling, when the couple $\{\lfloor \omega_1^\ell \rfloor_j^{n+1}, T_j^{n+1}\}$ intersects the liquidus curve, then the ice fraction passes from zero to a positive value. The system to solve comprises the three equations (35)–(37); eliminating $\lfloor \omega_3^+ \rfloor_j^{n+1}$ and then T_j^{n+1} from the system leads to a third-order polynomial equation with variable $\lfloor \omega_1^\ell \rfloor_j^{n+1}$, the roots of which are known. Let us stress here that the order of such polynomial equation to be finally solved is highly dependent on the order of the liquidus curve equation (Eq. (20)), and also on the assumptions (A4) and (A7).

All the physical properties used in the model are detailed in Appendix B.

3. Experiments

Fig. 2 presents the experimental apparatus used to study the coupled mass and heat transport in a *glass bead bed* saturated with a dilute water–*NaCl* solution ($\omega_{1_0}^\ell \in [0.01; 0.03]$, $T_0 \in [10; 30°\mathrm{C}]$) and in contact with a highly concentrated water–NaCl solution ($\omega_{1_\infty}^\ell = 0.234$, $T_\infty \leqslant T_0$). The experimental apparatus and procedures are briefly described below and the reader is referred to the paper of Lucas et al. [12] for further details.

The bed of 200-μm glass beads was contained in a plastic box (13 cm × 10 cm × [4; 10] cm). The porosity of the porous medium was assessed experimentally and found to be 0.428 ± 0.009. The porosity mean value approximated to 0.43 was used for main simulations presented; however when porosity measurement and

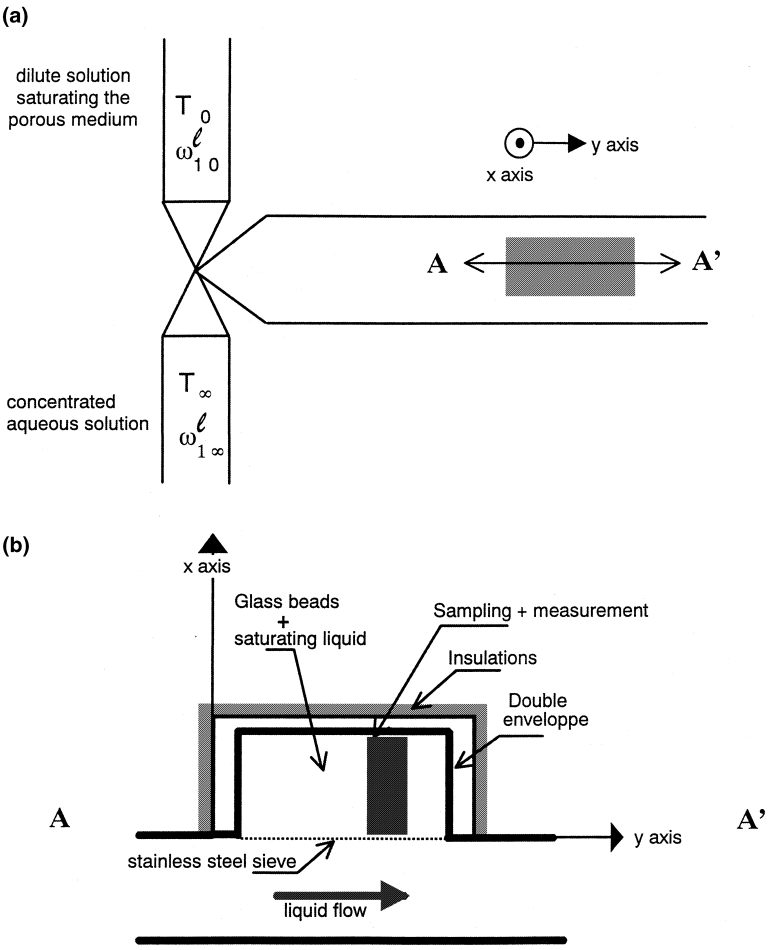

Fig. 2. Schematic diagram of the experimental apparatus: (a) view from above; (b) cross-section following the segment A–A′ as drawn in (a).

heat and mass transfer experiment were conducted on the same glass bead bed, the particular value of the porosity was used. The bottom of the box was limited by a stainless steel sieve (mesh size = 50 μm). The other sides of the plastic box were insulated. Mass and thermal resistance of the sieve were considered to be negligible. The size of the beads was adjusted to avoid capillarity phenomena and natural convection at the interstices. The bottom of the porous medium was placed above the duct of water–NaCl solution. The flow in the duct was set at 700 l h^{-1} and the corresponding h value was assessed experimentally using non-steady state measurements [12]. Within the measurement area – $y \in [75;110$ mm], $z \in [35;65$ mm], h was 500 W m^{-2} K^{-1}. Inside the glass bead bed in this area, temperature measurements were collected by previously standardised T-type thermocouples and the water–NaCl solution was sampled using the needles (1 mm external diameter) already in the bed. The NaCl concentration of the sampled liquid fraction was then determined with a chlorimeter (CORNING 926).

4. Results and discussion

4.1. Isothermal mass transport

Fig. 3 compares the experimental profiles of NaCl concentration in the porous medium ($\varepsilon = 0.4$) and the profiles predicted both by our model and using the analytical solution of the Fick equation proposed by Crank [13] in the case of a flat sheet $0 < x < 0.1$ m of uniform initial concentration and temperature ($\omega^{\ell}_{1_0} = 0.01$, $T_0 = 20°C$) in isothermal contact with a concentrated water–NaCl solution ($\omega^{\ell}_{1_\infty} = 0.234$, $T_\infty = 20°C$).

Preliminary simulations with our model using a constant diffusion coefficient gave profiles that fitted

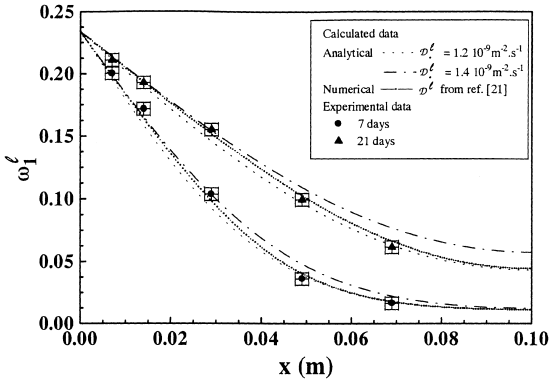

Fig. 3. NaCl profiles in a glass bead bed ($\omega^{\ell}_{1_0} = 0.01$, $T_0 = 20°C$, $\varepsilon = 0.4$, $L = 0.1$ m) in contact with a water–NaCl solution ($\omega^{\ell}_{1_\infty} = 0.234$, $T_\infty = 20°C$, $h = 500$ W m^{-2} K^{-1}). Experiment and simulations with analytical and numerical models.

perfectly the analytical solution calculated for the same diffusion coefficient value. The simulations with the numerical model represented in Fig. 3 were carried out taking into account a tortuosity of π/2 and changes in the diffusion coefficient, $D^{\ell}_{1/2}$, as a function of concentration and temperature (see Appendix B). Good agreement was noted between the experimental results and those simulated by the numerical model. When the model was used for diffusion alone, it gave a good representation of mass transport. This also confirms that no convection has been developed within the porous medium. With respect to mass transport, convection can result from the fact that the flow of water does not equal the flow of solute. Such case is encountered during immersion treatments of food matrix (deformable, of non-inert squeleton) such as the immersion freezing or the osmotic dehydration processes.

In Fig. 3, the analytical solution [13] is calculated for two constant values of $D^{\ell}_{1/2}$($D^{\ell}_{1/2} = 1.40 \times 10^{-9}$ and 1.20×10^{-9} m^2 s^{-1}). These correspond to the limits of the range of variation of $D^{\ell}_{1/2}$ (variation of ω^{ℓ}_1 from zero to saturation at 20°C), the equivalent of a ±15% variation. The two profiles calculated using the analytical solutions [13] are situated on either side of the profile simulated by the numerical model. These results all validated the calculation code for isothermal mass transport. Overall, an uncertainty of 15% for the value of the diffusion coefficient made it possible to roughly delimit the experimental error for the NaCl distribution profiles. Experimental uncertainty was primarily linked to the sampling volume (equivalent to a sphere 1.5 mm in diameter) [12], as represented on the x-axis in Fig. 3. In the following simulations, the coefficient of mutual diffusion for water and NaCl is therefore assumed to be constant and equal to the value of the diffusion coefficient at infinite dilution, $D^{\ell}_{1/2_\bullet}$. The experimental uncertainty on ω^{ℓ}_1 also did not allow any refinement of the identification of the tortuosity parameter, which is kept at π/2 in the following simulations.

4.2. Heat transport without phase change, with no mass transfer

Fig. 4 compares the experimental temperature profiles within the porous medium ($\varepsilon = 0.43$) and the profiles predicted both by our model and using the analytical solution of the Fourier equation proposed by Carslaw and Jaeger [14] in the case of a flat sheet $0 < x < 0.045$ m of uniform initial temperature and concentration ($\omega^{\ell}_{1_0} = 0.01$, $T_0 = 30°C$) in indirect contact with a water–NaCl solution ($T_\infty = 9.8°C$, $h = 500$ W m^{-2} K^{-1}). The bead bed was separated from the external solution (the refrigerating medium) by a metal sheet (thickness 0.2 mm). The thermal resistance of the sheet was negligible in comparison with the convective resistance of the external solution and the conductive resistance of the bead bed.

There was a perfect fit between the profiles simulated by the model and those calculated from the analytical solution of Carslaw and Jaeger [14]. This agreement validated the calculation code for heat transport without phase change with no mass transfer. Quite a good agreement was also noted between the simulated and the experimental results. This appeared to confirm the conductive nature of the heat transfer occurring within the bead bed.

4.3. Heat transport with phase change with no mass transfer

Fig. 5 compares the experimental changes, as a function of time, of the temperature at 5 positions (2,

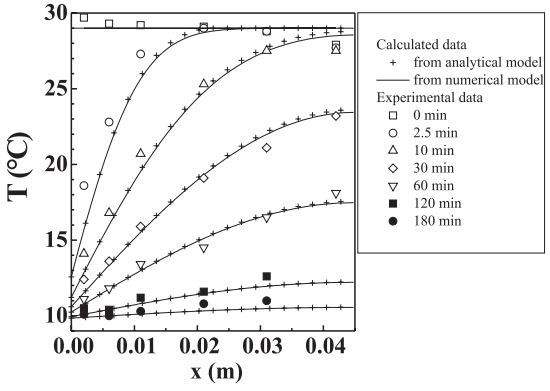

Fig. 4. Temperature profiles at various times during the cooling of a porous medium ($\omega^{\ell}_{1_0} = 0.01$, $T_0 = 30°C$, $\varepsilon = 0.43$, $L = 0.045$ m) in contact with a cold plate ($T_\infty = 9.8°C$, $h = 500$ W m^{-2} K^{-1}). Experiment and simulations with analytical and numerical models.

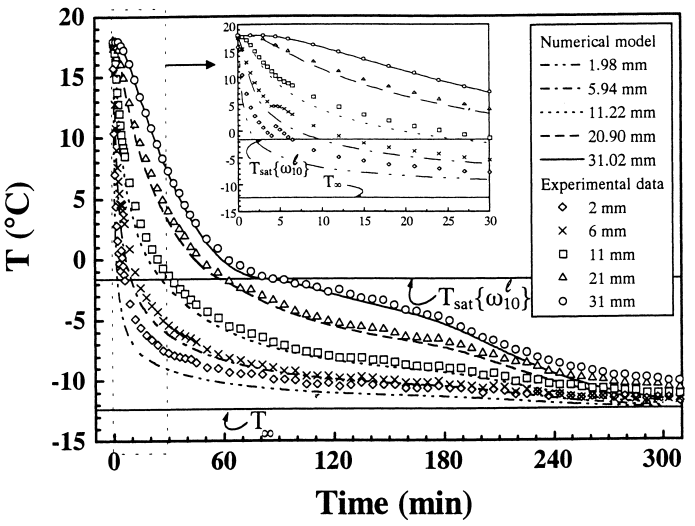

Fig. 5. Time–course changes in temperature (2, 6, 11, 21 and 31 mm) during the freezing of a porous medium ($\omega_{1_0}^{\ell} = 0.0305$, $T_0 = 17.9°C$, $\varepsilon = 0.43$, $L = 0.045$ m) in indirect contact with a concentrated water–NaCl solution ($T_\infty = -12.4°C$, $h = 500$ W m^{-2} K^{-1}). Confrontation of experimental and simulated (numerical model) data.

6, 11, 21 and 31 mm) within the porous medium ($\varepsilon = 0.43$) and the changes predicted by our model in the case of a flat sheet $0 < x < 0.045$ m of uniform initial concentration and temperature ($\omega_{1_0}^{\ell} = 0.0305$, $T_0 = 17.9°C$) in indirect contact with a concentrated water–NaCl solution ($T_\infty = -12.4°C$, $h = 500$ W m^{-2} K^{-1}).

There was good agreement between the experimental temperature data and those predicted by the model at the 21 and 31 mm positions. At the 2 and 6 mm positions, on the other hand, the simulated temperatures were lower than the experimental temperatures from 4 min onwards, by a maximum of 5°C. This discrepancy is the consequence of Assumption (A4) which consider the densities of water and ice equal, and of Assumption (A2) (local thermodynamic phase equilibrium) which does not allow the model to represent the supercooling phenomena. The supercooling noted near the surface (not represented in the figure) in fact slowed the rate of cooling to at least 11 mm depth. Despite such retardation phenomena, the model reflected the overall shape of the freezing kinetics well. The model gave a good simulation of the experimental data for most of the freezing and thus appeared to predict the overall duration of freezing correctly in the bead bed.

Let us precise that all the data usefull for the simulations of heat transport alone originated from experimental literature (h, ε, λ_i, C_i, ρ_i). The good agreement between the simulated data and the experimental data, obtained with or without phase change, validate the model used for the thermal conductivity of the porous medium.

4.4. Simultaneous heat and mass transport over long treatment times

Thawing and impregnation mechanisms inherent in the model: illustrations. Figs. 6 and 7 show the time–course changes in the calculated NaCl mass fraction relative to the liquid phase, ω_1^{ℓ} and to the ice–liquid mixture, ω_1^{+}, and in the calculated ice mass fraction relative to the ice–liquid mixture, ω_3^{+}, within a porous medium ($\omega_{1_0}^{\ell} = 0.03$, $T_0 = 20°C$, $\varepsilon = 0.4$, $L = 0.04$ m) in contact with a concentrated water–NaCl solution ($\omega_{1_\infty}^{\ell} = 0.21$, $T_\infty = -12°C$, $h = 400$ W m^{-2} K^{-1}) for $t < 10$ h and $t < 12$ days, respectively.

For any point in the porous medium far enough from the surface (e.g. 13 mm in Figs. 6 and 7), the kinetics of $\omega_1^{\ell}, \omega_1^{+}$ and ω_3^{+} can be broken down into three phases. During the first phase (I), most of the heat transport occurs without solute diffusion: $\omega_1^{+} = \omega_{1_0}^{\ell} = \text{const}$ (Fig. 7). Thermal equilibrium is reached in about 4 h. The amount of frozen water, $\omega_{3_{max}}^{+}$, is then maximal for the given operating conditions; in the absence of mass transfer, this amount (81% in Figs. 6 and 7) is determined by T_∞ and $\omega_{1_0}^{+}$. Additionally the increase in the NaCl mass fraction in the liquid phase up to saturation concentration is solely the effect of cryoconcentration. During the second phase (II), e.g. from 8.8 days for $x = 13$ mm (Fig. 7), NaCl arrives by diffusion ($\omega_1^{+} > \omega_{1_0}^{\ell}$) and causes the ice crystals to melt (ω_3^{+} decreases). The melted water dilutes the liquid phase in accordance with the thermodynamic equilibrium curve of the liquidus. For example, in such conditions, for 16 g of NaCl transported by diffusion in this region, 84 g of ice melts. This is important to understand that while all

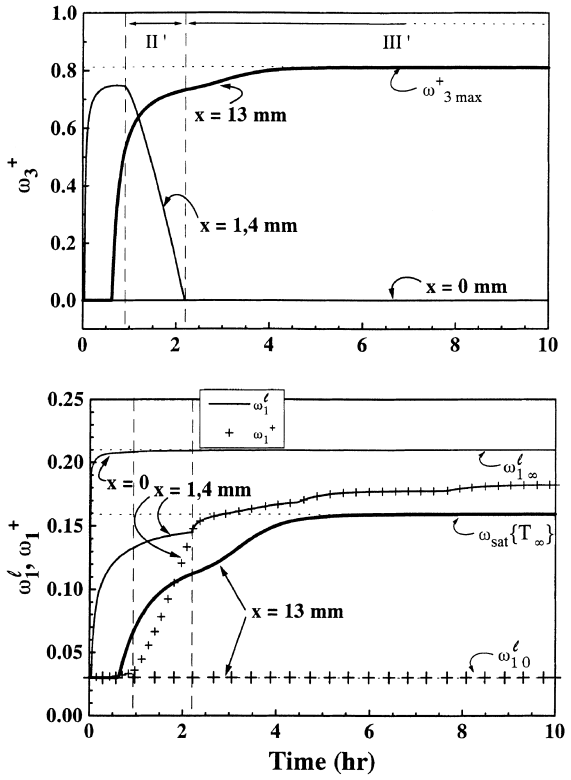

Fig. 6. Changes over time in simulated NaCl ($\omega_1^{\ell}, \omega_1^{+}$) and ice ($\omega_3^{+}$) fractions in a glass bead bed ($\omega_{1_0}^{\ell} = 0.03$, $T_0 = 20°C$, $\varepsilon = 0.4$, $L = 0.04$ m) in contact with a water–NaCl solution NaCl ($\omega_{1_\infty}^{\ell} = 0.21$, $T_\infty = -12°C$, $h = 400$ W m^{-2} K^{-1}) for a 10-h simulation. Refer to the text for $\omega_{3_{max}}^{+}$ signification.

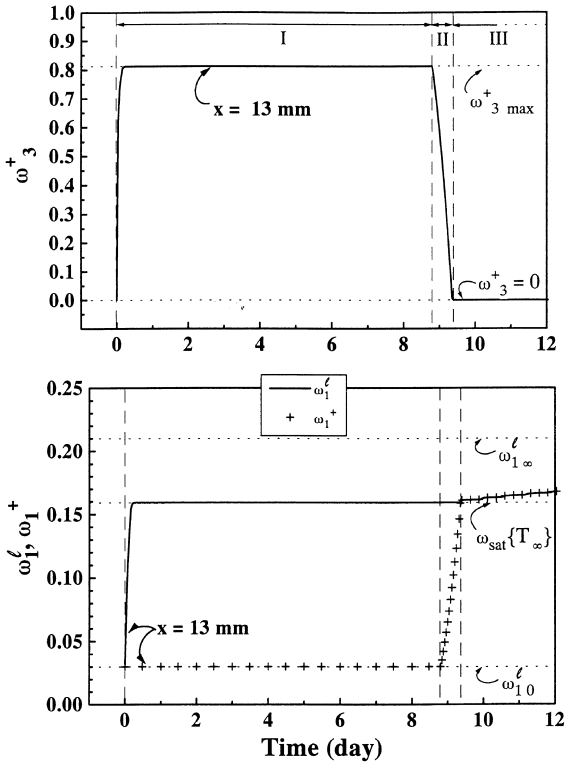

Fig. 7. Changes over time in simulated NaCl ($\omega_1^{\ell}, \omega_1^{+}$) and ice ($\omega_3^{+}$) fractions in a glass bead bed ($\omega_{1_0}^{\ell} = 0.03$, $T_0 = 20°C$, $\varepsilon = 0.4$, $L = 0.04$ m) in contact with a water–NaCl solution ($\omega_{1_\infty}^{\ell} = 0.21$, $T_\infty = -12°C$, $h = 400$ W m^{-2} K^{-1}) for a 12-day simulation. Refer to the text for $\omega_{3_{max}}^{+}$ signification.

the ice has not melt at $x = 13$ mm, the solute does not penetrate deeper in the partially frozen region ($x > 13$ mm). Once all the ice has melted (i.e. at 9.4 days in Fig. 7) the third phase (III) begins. NaCl transport continues and only NaCl concentration in the liquid phase increases at $x = 13$ mm. In other words, the situation is one of simple isothermal mass diffusion (at T_∞) in the liquid phase ($\omega_1^{+} = \omega_1^{\ell}$). The very beginning of phase (III) at $x = 13$ mm corresponds to the start of phase (II) in the next node ($x + \Delta x$).

Close to the interface, earlier interactions between heat and mass transfer occur. As illustrated at $x = 1.4$ mm in Fig. 6, solute arrives (at $t = 1$ h) while thermal equilibrium has not yet been reached ($\omega_3^{+} = 0.76 < \omega_{3_{max}}^{+}$): strictly speaking, one cannot define the previously observed phase (I) at this considered point in the porous medium. The ice starts to melt (equivalent phase II, noted phase II' in Fig. 6) while the temperature of the medium falls. This occurs independently of cryoconcentration, which continues (ω_1^{ℓ} is still increasing while ice melting). After 2 h, all ice crystals have melted. Fig. 6 additionally shows that the surface did not freeze at all ($\omega_3^{+} = 0\ \forall t$), and NaCl concentration quickly approaches that of the external solution, $\omega_{1_\infty}^{\ell}$. Other study showed that the total absence of freezing could even apply to thin layers beneath the surface of the porous medium [15].

The melting of the ice crystals reproduced by the numerical model covers only one space element at a time, thus suggesting the advance of a (localised) thawing front separating a completely thawed region from a region that is either frozen or in the process of freezing (this phenomenon is well illustrated in Fig. 9 presented in Section 4.5). The same phenomenon has been observed for other simulation configurations, in particular where $\omega_{1_0}^{\ell}$ is variable.

All these mechanisms appear in part similar to the assumptions serving as the basis for the analytical approach developed by Harrison and Osterkamp [9] and others, and presented in Section 1. The following section compares the simulations of these two models with a set of experimental data.

4.5. Experimental validation using a glass bead bed

Fig. 8 compares the experimental advance of the thawing front over 50 days with that simulated by the numerical model and the analytical model of Harrison and Osterkamp [9] for a glass bead bed ($\omega^{\ell}_{1_0} = 0.0305$, $T_0 = 17.7°C$, $\varepsilon = 0.43$, $\tau = \pi/2$, $L = 0.045$ m) in contact with a water–NaCl solution ($\omega^{\ell}_{1_\infty} = 0.234$, $T_\infty = -12.4°C$, $h = 500$ W m^{-2} K^{-1}). The advance of the thawing front predicted by the analytical model is given by

$$X\{t\} = \left[\frac{1}{2}\left(\frac{T_{\mathrm{sat}}\{\omega^{\ell}_{1_\infty}\}}{T_\infty} - 1\right)\right]^{1/2}\sqrt{4\frac{D^{\mathrm{m}}_{1/2}}{\varepsilon}t}. \tag{38}$$

The experimental advance of the thawing front was indirectly monitored when sampling was carried out at the points where the needles were situated: once the porous medium had started to freeze, it rapidly became impossible to sample the liquid phase because of the small amount of remaining solution. Sampling again became possible once the thawing front passed a given needle, thus allowing discontinuous monitoring of the advance of the thawing front. Attempts at sampling were made as often as possible at the points where the three needles had been placed in the bead bed ($x = 8$, 13, 28 mm). Sampling was again possible at these points at $t = 1.9$, 5.9 and 47 days, respectively, and later [12].

It is apparent that the numerical model satisfactorily reproduced the evolution of the thawing front observed in the bead bed. The advance of the thawing front predicted by the analytical model was faster than that predicted by the numerical model: the thickness of the thawed layer predicted by the analytical model was in this case 40–50% greater than that predicted by the numerical model. This can doubtless be attributed to the fact that the analytical model did not take account of the marked nonlinearity of the liquidus curve ω^{ℓ}_1 linked to T.

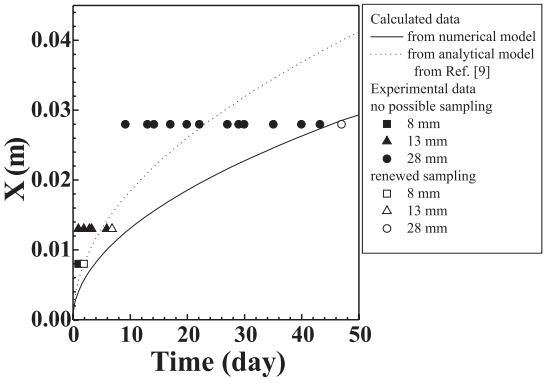

Fig. 8. Comparison (over 50 days) of the experimental advance of the thawing front and the advance simulated by our numerical model and the analytical model of Harrison and Osterkamp [9], for a porous medium made of glass beads ($\omega^{\ell}_{1_0} = 0.0305$, $T_0 = 17.7°C$, $\varepsilon = 0.43$, $L = 0.045$ m) in contact with a water–NaCl solution ($\omega^{\ell}_{1_\infty} = 0.234$, $T_\infty = -12.4°C$, $h = 500$ W m^{-2} K^{-1}). Experimental data taken from [12].

Fig. 9 presents the profile of the experimental NaCl mass fraction in the liquid phase [12] and that calculated by the numerical model within a bead bed in contact with a water–NaCl solution for the same conditions as in Fig. 8 and for different days: 6, 15 and 30 days. The ice fraction profile calculated for the same conditions is also presented in each figure, to localise the thawing 'front'.

In Fig. 9, the sampling position at $x = 13$ mm (the first sample possible at this point) coincides at $t = 6$ days with the position of the thawing front predicted by the numerical model: it is apparent that, at the start of phase III, concentration in the liquid phase was close to the value for $\omega_{\mathrm{sat}}\{T_\infty\}$ predicted by the thermodynamic equilibrium between the liquid and ice phases. Once the glass bead bed had thawed at a given point, the experimental NaCl content increased over time (as shown for instance at $x = 13$ mm in Fig. 9 at $t = 15$ and 30 days), and this was reproduced quite well by the model in quantitative terms. The number of experimental points was insufficient, however, to validate the linearity of the NaCl content profile simulated by the numerical model.

5. Conclusion

The one-dimensional numerical simulations of porous medium freezing in contact with a concentrated aqueous solution give the changes in solute concentration, ice fraction and temperature fields against time. They reproduce very satisfactorily the experimental results obtained with the glass bead bed. The model was verified for both heat and mass transfer, both coupled and without coupling, over wide ranges of temperature (30°C to −12.4°C) and solute concentration (0.01–0.234). All physical and transport property values used in the simulations were taken from the literature or previously measured by the authors (porosity and heat transfer coefficient). In the application case of the immersion freezing process, the model demonstrated the existence of two regimes of solute impregnation closely linked to ice formation:

1. At the start of the process, solute diffusion can be fast enough to prevent any freezing whatsoever at the interface, and to enhance the thawing of recently 'frozen' layers. This results in a non-frozen surface layer forming within the time necessary to reach thermal equilibrium at core of the porous medium.

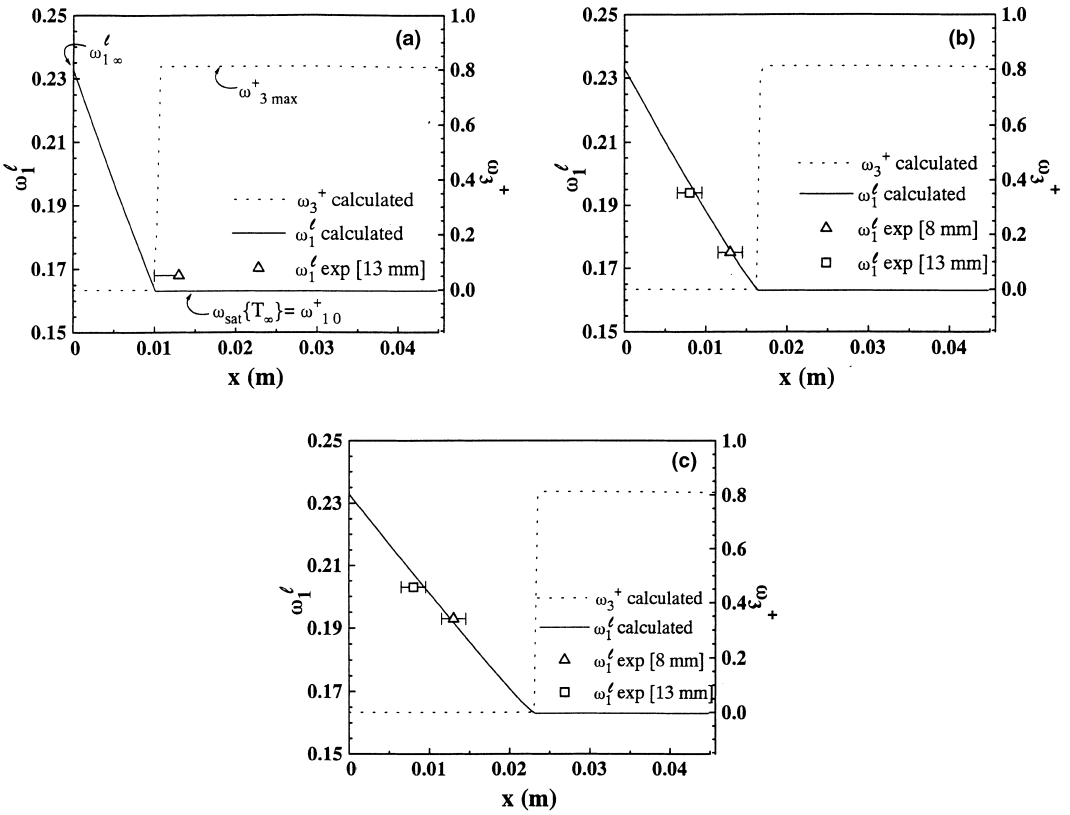

Fig. 9. Experimental ($x = 8$, 13 and 28 mm) profiles of the NaCl mass fraction in the liquid phase and profiles of both the ice fraction and NaCl mass fraction calculated by the numerical model, within a bead bed ($\omega^{\ell}_{1_0} = 0.0305$, $T_0 = 17.7$°C, $\varepsilon = 0.43$, $L = 0.045$ m) in contact with a water–NaCl solution ($\omega^{\ell}_{1_\infty} = 0.234$, $T_\infty = -12.4$°C, $h = 500$ W m^{-2} K^{-1}) at (a) 6 days, (b) 15 days and (c) 30 days. Experimental data taken from [12].

2. Continuous solute diffusion in the non-frozen layers causes the adjacent ice crystals to melt (local equilibrium condition). This would persist until mass equilibrium between the liquid phases of the porous medium and the external solution has been reached. The final equilibrium state of the porous medium is conditioned by the characteristics of the refrigerating external solution: with monophasic (liquid) freezants, the product thaws completely and its solute concentration approximates that of the solution.

Appendix A. Expression of coefficients A_j^n and $B^n_{i\in[1,2,3,4],j}$

$$B_1 = (1-\varepsilon)\rho_4 C_4 + \varepsilon\rho_\ell C_\ell,$$

$$B_2 = \varepsilon\rho_\ell C_3 - \rho_\ell C_\ell,$$

$$B_3 = \varepsilon\rho_\ell\,\Delta H.$$

• for $1 < j < j\max$

$$\begin{aligned} B^n_{4_j} = {} & \frac{\Delta t}{\Delta x^2}\Big\{[k_{\mathrm{m}}]^n_{j+1/2}\Big(T^n_{j+1} - T^n_j\Big) \\ & + [k_{\mathrm{m}}]^n_{j-1/2}\Big(T^n_{j-1} - T^n_j\Big)\Big\} + T^n_j\Big\{(1-\varepsilon)\rho_4 C_4 \\ & + \varepsilon\rho_\ell C_3\big[\omega_3^+\big]^n_j + \varepsilon\rho_\ell C_\ell\big(1 - \big[\omega_3^+\big]^n_j\big)\Big\} \\ & - \varepsilon\rho_\ell \Delta H\big[\omega_3^+\big]^n_j, \end{aligned}$$

$$\begin{aligned} A^n_j = {} & (1 - \lfloor\omega_3^+\rfloor^n_j)\lfloor\omega_1^\ell\rfloor^n_j \\ & + \frac{\Delta t}{\Delta x^2}\left\{\frac{\big[D^\ell_{1/2}\big]^n_{j+1/2}}{\tau}\Big(1 - \big[\omega_3^+\big]^n_{j+1/2}\Big)\Big(\big[\omega_1^\ell\big]^n_{j+1} - \big[\omega_1^\ell\big]^n_j\Big)\right. \\ & \left. + \frac{\big[D^\ell_{1/2}\big]^n_{j-1/2}}{\tau}\Big(1 - \big[\omega_3^+\big]^n_{j-1/2}\Big)\Big(\big[\omega_1^\ell\big]^n_{j-1} - \big[\omega_1^\ell\big]^n_j\Big)\right\}. \end{aligned}$$

• for $j=1$:

$$B^n_{4_{j=1}} = \frac{\Delta t}{\Delta x^2}\left\{[k_{\mathrm{m}}]^n_{j=3/2}\left(T^n_{j=2}-T^n_{j=1}\right) + \frac{\Delta t}{\Delta x}h\left(T_\infty - T^n_{j=1/2}\right)\right\} + T^n_{j=1}\left\{(1-\varepsilon)\rho_4 C_4 + \varepsilon\rho_\ell C_3\left[\omega_3^+\right]^n_{j=1} + \varepsilon\rho_\ell C_\ell\left(1-\left[\omega_3^+\right]^n_{j=1}\right)\right\} - \varepsilon\rho_\ell\Delta H\left[\omega_3^+\right]^n_{j=1},$$

$$A^n_{j=1} = \left(1-\left[\omega_3^+\right]^n_{j=1}\right)\left[\omega_1^\ell\right]^n_{j=1} + \frac{\Delta t}{\Delta x^2}\left\{\frac{\left[D^\ell_{1/2}\right]^n_{j=3/2}}{\tau}\left(1-\left[\omega_3^+\right]^n_{j=3/2}\right)\left(\left[\omega_1^\ell\right]^n_{j=3/2} - \left[\omega_1^\ell\right]^n_{j=1}\right)\right\} + \frac{\Delta t}{\Delta x}\frac{\rho_\infty K}{\rho_\ell \varepsilon}\left(\left[\omega_1^\ell\right]_\infty - \left[\omega_1^\ell\right]^n_{j=1/2}\right).$$

• for $j = j\max$:

$$B^n_{4_{j\max}} = \frac{\Delta t}{\Delta x^2}[k_{\mathrm{m}}]^n_{j\max+1/2}\left(T^n_{j\max+1}-T^n_{j\max}\right) + T^n_{j\max}\left\{(1-\varepsilon)\rho_4 C_4 + \varepsilon\rho_\ell C_3\left[\omega_3^+\right]^n_{j\max} + \varepsilon\rho_\ell C_\ell(1-\left[\omega_3^+\right]^n_{j\max})\right\} - \varepsilon\rho_\ell\Delta H\left[\omega_3^+\right]^n_{j\max},$$

$$A^n_{j\max} = \left(1-\left[\omega_3^+\right]^n_{j\max}\right)\left[\omega_1^\ell\right]^n_{j\max} + \frac{\Delta t}{\Delta x^2}\left\{\frac{\left[D^\ell_{1/2}\right]^n_{j\max+1/2}}{\tau}\left(1-\left[\omega_3^+\right]^n_{j\max+1/2}\right) \times\left(\left[\omega_1^\ell\right]^n_{j\max+1} - \left[\omega_1^\ell\right]^n_{j\max}\right)\right\}.$$

• for $j=1/2$ ($x=0$):

Temperature and concentration at the system surface were deduced assuming a quadratic profile, respectively, in temperature and concentration, e.g.

$$\left(T^n_{j\in[1,2]} - T^n_{j=1/2}\right) = \gamma x + \delta x^2.$$

Further details on the calculation can be obtained in [16].

Appendix B. Numerical values of physical parameters

• Density and specific heat capacity at constant pressure

Component (i)	ρ_i^i (kg m^{-3})	C_i (J kg^{-1} K^{-1})
liquid (ℓ) (water + solute)	1000	4180
Ice (3)	1000	2900
Glass beads (4)	2700	800

• Effective thermal conductivity k_{m} (W m^{-1} K^{-1}) (from Ref. [17])

$$k_{\mathrm{m}} = (k_4)^{\rho_4(1-\varepsilon)}(k_3)^{\rho_3\varepsilon\omega_3^+}(k_\ell)^{\rho_\ell\varepsilon(1-\omega_3^+)},$$

where k_i is the thermal conductivity of component i (W m^{-1} K^{-1}) and value is taken from the literature [18–20]

$$k_3 = 0.4685 + [488/(T+273.15)],$$
$$k_4 = 1.16,$$
$$k_\ell = (0.57 - 0.64\omega_l^\ell) + (1.14\times10^{-3} - 2\times10^{-3}\omega_1^\ell)T.$$

• Effective diffusion coefficient of NaCl $D^{\mathrm{m}}_{1/2}$ (m^2 s^{-1})

$$D^{\mathrm{m}}_{1/2} = \frac{D^\ell_{1/2}}{\tau},$$

where τ is the tortuosity or the relative increase in the transport of molecules through the liquid phase due to the presence of the solid matrix of the porous medium and the presence of ice crystals ($\tau=\pi/2$). Please note that the tortuosity is assumed to be independent on the ice fraction (spherical ice crystals of diameter similar to glass beads) (A11). However the obstruction to transport associated with the ice crystals is taken into account in the mass diffusivity. $D^\ell_{1/2}$ is the mutual diffusion coefficient of water and NaCl. Data for $D^\ell_{1/2}$ for ($T<10$°C) are not available in the literature. This coefficient was calculated from the correlation established by Bohuon [21] at 20°C

$$D^\ell_{1/2}/D^\ell_{1/2_\bullet} = 1 - 0.3869\sqrt{m_1} + 0.274m_1 - 0.0197m_1^2,$$

where m_1 is the NaCl molality (mol kg^{-1} of solvant). $D^\ell_{1/2_\bullet}$ is the mutual diffusion coefficient of water and NaCl at infinite dilution and was estimated using the Stokes–Einstein relation [22] for $T=20$°C: $(D^\ell_{1/2_\bullet}\cdot\mu_2)/(T+273.15) = \text{const}$, where μ_2 is the dynamic viscosity of water and T is the temperature. The dynamic viscosity of water for $-12<T<0$°C is assumed to be the same as the viscosity of supercooled water, on the basis of the data presented by Ref. [23].

• Latent heat of fusion of ice at 0°C:

$$\Delta H = 334\times10^3 \text{ (J kg}^{-1}\text{)}.$$

• Liquidus curve equation: the fitted liquidus curve was determined according to experimental data from literature [20]

$$T_{\mathrm{sat}} = -0.027 - 46.30\,\omega_1^\ell - 182.02(\omega_1^\ell)^2.$$

- When comparing the simulated and experimental data, the porosity of the porous medium and the overall heat transfer coefficient values used were those assessed experimentally (refer Section 3).
- Heat and mass transfer at the interface porous medium/external solution are coupled by assuming a Chilton–Colburn analogy. Mass and heat transfer coefficients are then linked by the following relation:

$$K = h\frac{D^{\ell}_{1/2_\bullet}}{\lambda_\infty}\left[\frac{D^{\ell}_{1/2_\bullet}}{\alpha_\infty}\right]^{1/3}.$$

References

[1] K. Hutter, T. Alts, Ice and snow mechanics: a challenge to theorical and applied mechanics, Theorical and Applied Mechanics, Proceedings of the XVI International Congress, North-Holland, Amsterdam, 1985.

[2] H.T. Meryman, Cryobiology, first ed., Academic Press, London, 1966, pp. 66–69.

[3] T. Lucas, A.L. Raoult-Wack, Immersion chilling and freezing in aqueous refrigerating media: review and future directions, Int. J. Refrig. 21 (1998) 419–429.

[4] X. Li, Mathematical modeling of solute segregation and redistribution during freezing in peat and overlying water, Ph.D. thesis, University of Michigan, 1985, p. 107.

[5] M. Jochem, C. Korber, A numerical solution of the coupled heat and mass transfer problem of non-planar solidification and melting of aqueous solutions, Wärme- und Stoffübertragung 28 (1993) 195–204.

[6] M.G. O'callaghan, E.G. Cravalho, C.E. Huggins, An analysis of the heat and solute transport during solidification of an aqueous binary solution. I. Basal plane region, Int. J. Heat Mass Transfer 25 (1982) 553–561.

[7] M.G. O'callaghan, E.G. Cravalho, C.E. Huggins, An analysis of the heat and solute transport during solidification of an aqueous binary solution. II. Dendrite tip region, Int. J. Heat Mass Transfer 25 (1982) 563–573.

[8] V.J. Lunardini, Heat Transfer with Freezing and Thawing, Elsevier, Amsterdam, 1991, pp. 31–35.

[9] W.D. Harrison, T.E. Osterkamp, Heat and mass transport in subsea permafrost. 1. An analysis of molecular diffusion and its consequences, J. Geophys. Res. 83 (1978) 4707–4712.

[10] V.L. Vasil'ev, A.M. Maksimov, E.E. Petrov, G.G. Tsypkin, Mathematical model of the freezing-thawing of saline frozen soil, J. Appl. Mech. Technol. Phys. 36 (1995) 689–696.

[11] R.B. Bird, W.E. Stewart, E.N. Lightfoot, Transport Phenomena, first ed., Wiley, New York, 1960, p. 556–558, 651.

[12] T. Lucas, C. Favier, J.M. Chourot, J. Guilpart, A.L. Raoult-Wack, R. Ben Aim, ICF in refrigerating aqueous media: heat and mass transport in model food glass bead bed, Int. J. Food Sci. Technol. 35 (2000) 583–598.

[13] J. Crank, Free and Moving Boundary Problems, Oxford Science Publications, Oxford, 1982, p. 47.

[14] H.S. Carslaw, J.C. Jaeger, Conduction of Heat in Solids, second ed., Clarendon Press, Oxford, 1959, p. 126.

[15] T. Lucas, D. Flick, A.L. Raoult-Wack, Mass and thermal behaviour of the food surface during immersion freezing, J. Food Eng. 41 (1999) 23–32.

[16] T. Lucas, Réfrigération et congélation par immersion dans des liquides aqueux concentrés: caractérisation expérimentale et modélisation des transferts couplés de chaleur et de matière, Ph.D. thesis, ENGREF, Paris, France, 1998, p. 189.

[17] A.H. Lachenbruch, J.H. Sass, B.V. Marshall, T.H. Moses Jr., Permafrost, heat flow and the geometrical regime at Pudhoe Bay, Alaska, J. Geophys. Res. 87 (1982) 9301–9316.

[18] ASHRAE (Ed.), ASHRAE Handbook – 1981 Fundamentals, American Society of Heating, Refrigerating and Air-Conditioning Engineers Inc., Atlanta, GA, 1983, pp. S26.1–S26.8.

[19] P.V. Hobbs, Ice Physics, Clarendon Press, Oxford, 1974, pp. 357–361.

[20] R.H. Perry, C.H. Chilton (Eds.), Chemical Engineers' Handbook, McGraw-Hill, Kogakusha, Tokyo, 1973, pp. 23–60.

[21] P. Bohuon, Dehydration–impregnation by soaking treatments in ternary aqueous solutions: experimental characterization and modelling of water and solute transport inside gel and meat tissue (in French), Ph.D. thesis, University of Montpellier II (Fr), 1995, p. 216.

[22] E.L. Cussler, Diffusion: Mass Transfer in Fluid Systems, Cambridge University, New York, 1984.

[23] R.C. Weast (Eds.), Handbook of Chemistry and Physics, CRC Press, Boca Raton, Florida, 1987.